Applied Surface Science 584 (2022) 152585

Contents lists available at ScienceDirect

Applied Surface Science

journal homepage: www.elsevier.com/locate/apsusc

Full Length Article

# Oxygen-mediated selection of Cu crystallographic orientation for growth of single-crystalline graphene

Hyeong-ku Jo [a,b,c], Hanjin Park [d], Hyung-June Lee [d], Garam Bae [b], Da Som Song [b], Ki Kang Kim [c], Wooseok Song [b,*], Cheolho Jeon [e], Ki-Seok An [b], Young-Kyun Kwon [d,f,*], Chong-Yun Park [a,*]

[a] Department of Physics, Sungkyunkwan University, Suwon 16419, Republic of Korea
[b] Thin Film Materials Research Center, Korea Research Institute of Chemical Technology, Daejeon 34114, Republic of Korea
[c] Department of Energy Science, Sungkyunkwan University, Suwon 16419, Republic of Korea
[d] Department of Physics, Kyung Hee University, Seoul 02447, Republic of Korea
[e] Advanced Nano Surface Research Group, Korea Basic Science Institute, Daejeon 34133, Republic of Korea
[f] Department of Information Display and Research Institute for Basic Sciences, Kyung Hee University, Seoul 02447, Republic of Korea

ARTICLE INFO

*Keywords:*
Recrystallization
Single crystal
Cu foil
Graphene
Oxygen content

ABSTRACT

Grains of a polycrystalline Cu foil (CF) can be recrystallized into Cu(1 0 0) or Cu(1 1 1) by adequate thermal annealing near the surface melting temperature. However, the thermally driven recrystallization mechanism of CF remains elusive, which is connected to the uncontrollability of the orientation of recrystallized Cu surface. In this study, we ascertained that the unintentional presence of oxygen in CF grains acts a crucial role in determining the crystal orientation of CF. Comprehensive spectroscopic analysis coupled with density functional theory calculation was implemented to explore the correlation between the surface phase transition and the oxygen content of the surface of CFs. After annealing, oxygen-free Cu grains were explicitly recrystallized in the (1 1 1) crystal plane by minimizing their surface energy, whereas oxygen-contained Cu grains were recrystallized in the (1 0 0) orientation due to the elastic strain energy induced by oxygen. Notably, we arguably accomplished the recrystallized CF with (1 1 1) crystal plane can be transformed into a single crystal (1 1 1) CF by utilizing rationally designed cyclic heat treatment (CHT), however Cu(1 0 0) grains were not merged into a single crystal (1 0 0) CF presumably due to the presence of residual oxygen. We accomplished the synthesis of defect-less, continuous monolayer graphene on a single crystal (1 1 1) CF.

## 1. Introduction

A single-crystal Cu foil (CF) enables the epitaxial synthesis of a large-area high-quality graphene film without structural imperfection or grain boundaries (GBs) by chemical vapor deposition (CVD) because Cu(1 1 1) planes allow a small lattice mismatch with graphene of less than 4%. Hence, a single-crystal CF with (1 1 1) crystal plane is highly demanded for the growth of a large-area single-crystalline graphene film [1–3]. Unfortunately, a single-crystal Cu grown by conventional methods, such as the Czochralski and Bridgman methods, has been inevitably accompanied by a lack of large-area compatibility and production cost-effectiveness. As alternative approaches for obtaining large-area single-crystal CFs from commercially available polycrystalline CFs, thermal annealing methods have attracted a great deal of attention [4–8]. Thus far, diverse strategies involving chemical mechanical polishing, annealing, surface energy minimization, oxygen adsorption, surface oxidation, and capping layers have been implemented for the recrystallization of CFs [7–14]. Owing to the lack of in-depth studies, however, the universal mechanism for the recrystallization of CF remain elusive. In this study, we unprecedentedly explored the recrystallization process for Cu grains in a specific direction, in which the structural transition of Cu grains was mainly mediated by the oxygen content of the surface of Cu. Based on an in-depth exploration of the recrystallization phenomenon for oxygen-free CF, we ascertained thermally driven recrystallization in the (1 1 1) direction of CF grains induced by the surface phase transition to minimize the surface energy [9–11]. Additionally, we devised cyclic heat treatment (CHT) enabling that small grains with the (1 1 1) orientation merge into one huge grain, ultimately becoming a single crystal.

* Corresponding authors at: Department of Physics, Kyung Hee University, Seoul 02447, Republic of Korea (Y.-K. Kwon).
*E-mail addresses:* wssong@krict.re.kr (W. Song), ykkwon@khu.ac.kr (Y.-K. Kwon), cypark@skku.edu (C.-Y. Park).

https://doi.org/10.1016/j.apsusc.2022.152585
Received 2 August 2021; Received in revised form 18 January 2022; Accepted 21 January 2022
Available online 25 January 2022

## 2. Experimental and computational details

### 2.1. Preparation of CF recrystallized in preferential orientation

We examined the crystal structure of commercially available 25 μm-thick-CFs (CF1: 99.9%, Alpha Aesar, CF2: 99.999%, Alpha Aesar, CF3: 99.9%, oxygen-free SH copper product, Hitachi Metals, CF4: 99.9%, electrolytic tough pitch SH copper product, Hitachi Metals). The recrystallization procedure of CFs in preferential orientation was implemented by a conventional 1-inch tube furnace (Thermo Fisher Scientific, Lindberg Blue M HTF55322A, USA) with 225 sccm $H_2$ at 1050 °C for 2 h. The structural characterization was performed by XRD (MiniFlex600, Rigaku, Japan), TOF-SIMS (TOF-SIMS-5, IONTOF, Germany), and EBSD (JSM7000F, JEOL, Japan).

### 2.2. Synthesis of graphene on CFs

Graphene was synthesized by TCVD. The CF substrates were heated to 1050 °C inside the TCVD chamber with introducing $CH_4$ (0.32 and 1.5 sccm), $H_2$ (4 sccm), and Ar (40 sccm) under the pressure of ~550 Torr for 60 min, in which graphene coverage on CFs was precisely manipulated by regulating $CH_4$ flow rate.

### 2.3. Computational details

To investigate the oxygen effect on the structural stability of Cu surfaces and the role of CHT in the formation of one huge grain, we performed first-principles density functional theory (DFT) [15] calculations as implemented in Vienna *ab initio* simulation package (VASP) [16,17] and DFT-based Monte Carlo (MC) simulations. The electronic wavefunctions were expanded by plane-wave basis with a kinetic energy cutoff of 450 eV. We employed the projector-augmented wave pseudopotentials [18,19] to describe the valence electrons, and treated exchange–correlation (XC) functional within the generalized gradient approximation of Perdew-Burke-Ernzerhof (PBE) [20]. Atomic relaxation was performed until the Helmann-Feynman force acting on every atom became lower than 0.01 eV/Å., resulting in the equilibrium lattice constant of the bulk face-centered cubic structure to be 3.63 Å. We constructed various slab configurations composed of 72 or 108 Cu atoms distributed on 6 layers along either the [1 1 1] or [1 0 0] direction with a vacuum spacing of 20 Å along the out-of-plane direction to avoid the slab-slab interaction. Their corresponding Brillouin zones were sampled using a Γ-centered $3 \times 5 \times 1$ or $2 \times 4 \times 1$ mesh depending on the in-plane size according to the Monkhost-Pack scheme [21]. The detailed procedure of MC simulations is described in Supplementary Information.

## 3. Results and discussion

To explore thermally activated recrystallization phenomena of CF, as-received commercially available 25 μm-thick-CFs (CF1: 99.9% Alpha CF, CF2: 99.999% Alpha CF, CF3: 99.9% oxygen-free SH-CF, CH4: 99.9% electrolytic tough pitch SH-CF) were examined by electron backscatter diffraction (EBSD) coupled with X-ray diffraction (XRD), as presented in Fig. 1. Fig. 1(a–d) displays orientation distribution function (ODF) mapping acquired from EBSD of as-received CFs, revealing typical structural features of polycrystalline CFs containing small grains, irrespective of the samples. Inverse pole figure (IPF) maps for as-received CFs show randomly distributed crystallographic orientation, regardless of the sample, as shown in Fig. 1(e–h). For CF1, relatively larger grain and localized crystal planes are discernible. The discernible discrepancy in grains size and orientation for CFs relies on the manufacturing procedure of each CF. We prudently established annealing conditions for recrystallization of CFs; as-received CFs were annealed at 1050 °C with introducing 225 sccm $H_2$ for 2 h. The microstructural evolution of CFs after the annealing was implemented by EBSD combined with XRD. Two distinctive structural alterations can readily be discerned after the annealing: 1) the massive grain enlargement is distinctly attested after the annealing, as seen in Fig. 1(i–l) and Fig. S1. In particular, the sizes of grains for CF2 and CF3 were estimated to be 2 mm and 1.5 mm, respectively. 2) More intriguingly, we unambiguously ascertained thermally activated selection of crystallographic orientation containing (1 0 0) and (1 1 1) for CF2 and CF3 after the annealing [12–14]. Conversely, CF1 and CF4 possess a relatively broad distribution of crystallographic orientation after the annealing, as shown in Fig. 1(m–p). The prominent Bragg reflections of the (1 0 0) crystal plane for annealed CF2 and the (1 1 1) crystal plane for annealed CF3 gained from XRD analysis reinforce our findings from the EBSD results, as exhibited in Fig. 1(q–t). In general, the (1 1 1) crystallographic plane is energetically favorable with the lowest surface energy for the face-centered cubic (fcc) structure. Namely, polycrystalline fcc metals spontaneously transform into grains with a (1 1 1) surface with applying the activation energy for grain growth.

Notably, we traced that our findings correlated with abnormal surface recrystallization of CFs stem from the existence of oxygen in the CFs monitored by time-of-flight (TOF)-secondary ion mass spectroscopy (SIMS). Fig. 2(a, b) demonstrates SIMS depth profiles of oxygen for CF1, CF2, CF3, and CF4 with spilt analysis depth [22]. The presence of incorporated oxygen can be discriminated before the annealing, irrespective of the samples. The order of oxygen content is CF2 > CF4 > CF1 > CF3 near the surface of CFs (t = 0–50 nm). For CF4, approximately 1% oxygen compared to the oxygen concentration on the surface exists even at a depth of 300 nm. The established annealing procedure serves to an abrupt decline in the oxygen concentration, however, the order of oxygen content is retained (CF2 > CF4 > CF1 > CF3), as represented in Fig. 2(c). Based on these results, we can deduce that the annealing of oxygen-enriched CFs (CF2 and CF4) and oxygen-deficient CFs (CF3 and CF1) lead to the recrystallization of (1 0 0) and (1 1 1) crystal planes, respectively, which signals an oxygen mediated selection of crystallographic orientation of CFs, as illustrated in Fig. 2(d). To probe this hypothesis, we deliberately eliminated oxygen incorporated into CF2 and CF4 using an electro-polishing procedure before annealing the samples. A meaningful variation in the amount of oxygen near the electro-polished surface of CF2 and CF4 is discernible, as displayed in Fig. 2 (e, f). After polishing, the oxygen contents of CF2 and CF4 substantially decrease near the surface of CFs. For CF4, however, approximately 1% oxygen is still preserved at a depth of 300 nm, unlike CF2. As a result, a thermally activated structural transition from the (1 0 0) crystal plane induced by oxygen-enriched CFs to the (1 1 1) crystal plane is observed for electro-polished CF2, as exhibited in Fig. 2(g). Conversely, the (1 0 0) crystal plane is invariant for electro-polished CF4 because of the presence of incorporated oxygen at a depth of 300 nm, as presented in Fig. 2 (h). As mentioned earlier, the structural transition of Cu grains is highly correlated with the amount of oxygen into the grains. In the absence of oxygen, even though the strain energy density of (1 0 0)-oriented grains is lower than that of (1 1 1)-oriented grains, the grains undergo a structural transition to the (1 1 1) orientation at the surface with the lowest surface energy [9–14,22,23]. If incorporated oxygen remains near the surface, the surface of grains tends to be pinned as (1 0 0) orientation.

The oxygen-deficient CF3 contains large grains with the (1 1 1) orientation after annealing for 2 h, as displayed in Fig. 3(a). Although we prolonged the annealing time, the grains did not fully coalesce into a single crystal. Rather, annealing tended to cause along large grain boundaries. The grooves became deeper and wider with increasing annealing time, as seen in Fig. 3(b, c). Fig. 3(d) represents an average grain size of annealed CF3 as a function of annealing time, revealing that the grain size was estimated to be several micrometers to millimeters. The evolution of the grooves is attributable to a disparate sublimation behavior of Cu atoms at the grain and grain boundaries by high-temperature annealing, owing to boosted sublimation of Cu atoms at grain boundaries with structural instability. We can anticipate that

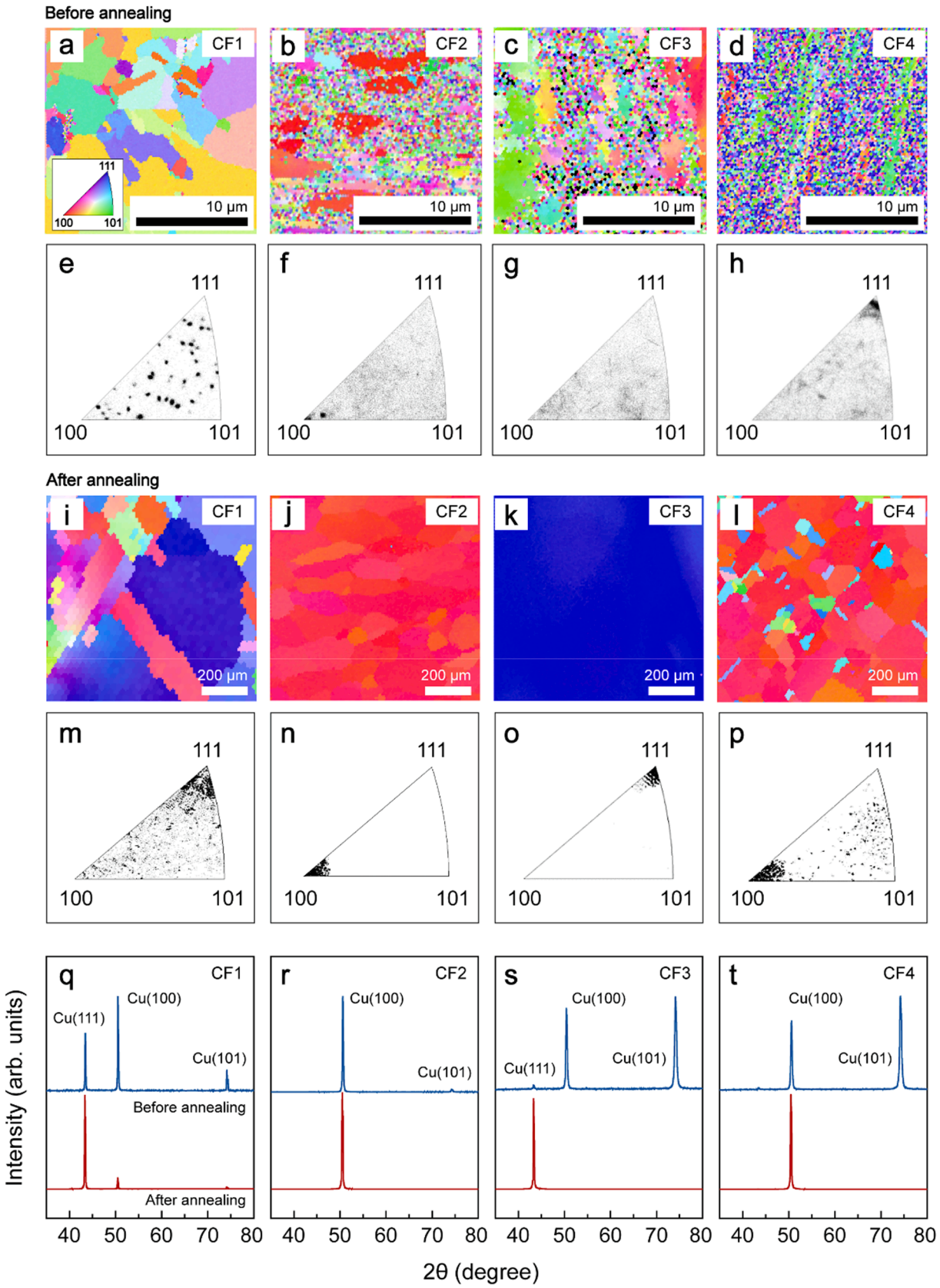


**Fig. 1.** Structural characterization of CFs before and after annealing. ODF and IPF maps acquired from EBSD for as-received (a, e) CF1, (b, f) CF2, (c, g) CF3, and (d, h) CF4. ODF and IPF maps acquired from EBSD for (i, m) CF1, (j, n) CF2, (k, o) CF3, and (l, p) CF4 after annealing with 225 sccm $H_2$ at 1050 °C for 2 h. XRD patterns for (q) CF1, (r) CF2, (s) CF3, and (t) CF4 before and after annealing.

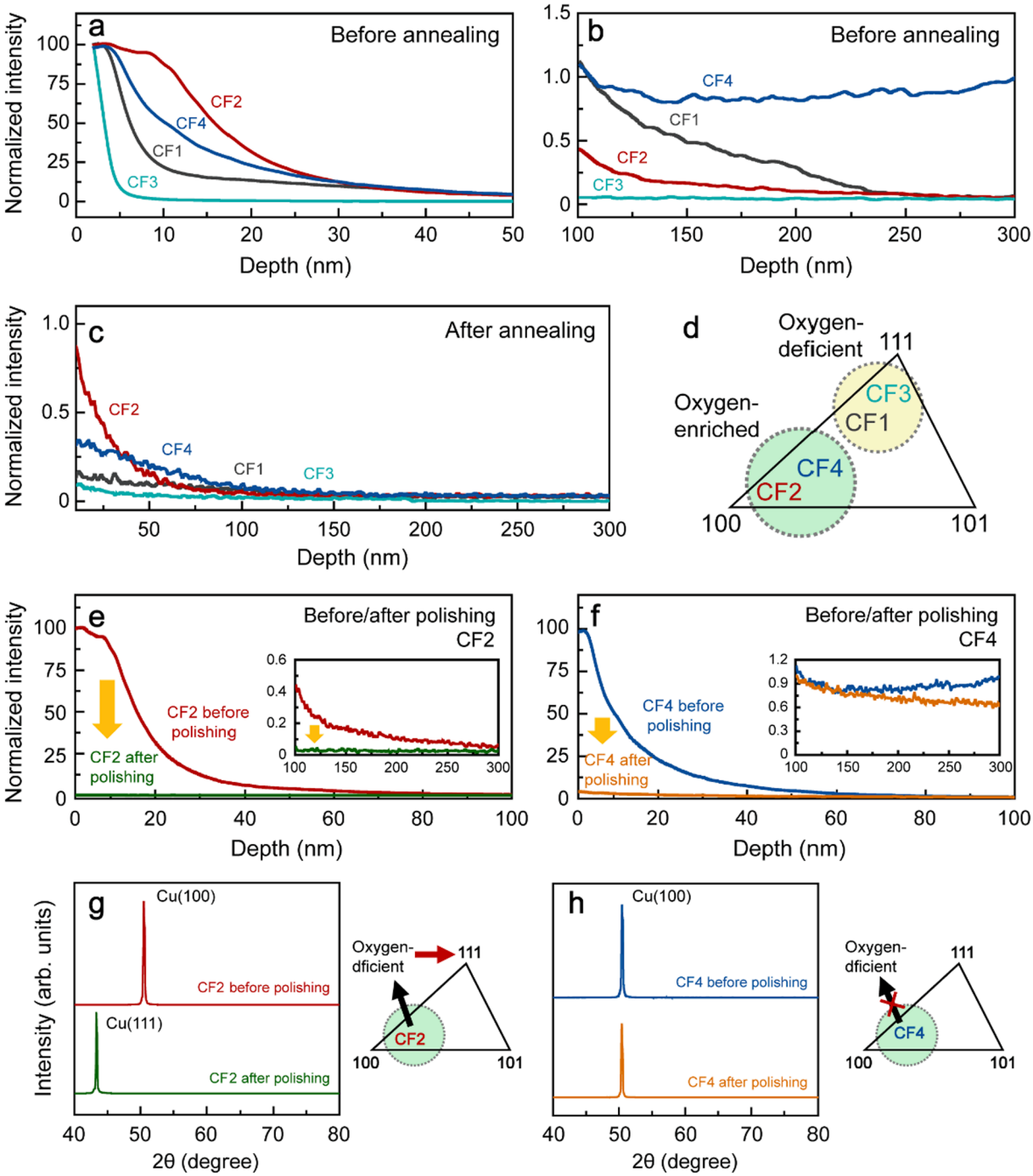


**Fig. 2.** A correlation between the surface recrystallization and the oxygen content of the surface of CFs. (a, b) SIMS depth profiles of oxygen for as-received CF1, CF2, CF3, and CF4 with split analysis depth (0–50 nm and 100–300 nm). (c) SIMS depth profiles of oxygen for CF1, CF2, CF3, and CF4 after annealing with 225 sccm $H_2$ at 1050 °C for 2 h. (d) A relationship between the crystallographic orientation and oxygen content of the surface of CFs. SIMS depth profiles of oxygen for as-received (e) CF2 and (f) CF4 before and after polishing. XRD patterns of (g) annealed CF2 and (h) annealed CF4 before and after polishing. Schematic representation of oxygen mediated selection of crystallographic orientation of CFs.

diffusion and sublimation of Cu atoms occur simultaneously at high temperatures. To understand the groove filling and widening processes experimentally observed during cyclic heat treatment (CHT), we performed Monte Carlo (MC) simulations based on density functional theory (DFT) calculation. It can be regarded that grooves would be filled when the reaching rate $\nu_s$ of Cu adatoms wandering on any domains of Cu (1 1 1) surface to any groove edges is higher than the escaping rate $\nu_e$ of dangling Cu atoms at any groove edges, whereas grooves would be widened if $\nu_s$ is lower than $\nu_e$. In other words, competition between these two rates would determine a dominant process during CHT. To evaluate $\nu_s$ and $\nu_e$, we computed the migration energy barrier $E_m$ of a Cu adatom between nearest neighboring fcc and hcp adsorption sites on a perfect Cu (1 1 1) surface, as shown in Fig. 4(a), and the escaping energy barrier $E_e$ of a dangling Cu atom from a groove edge binding site toward nearby adsorption sites on a Cu (1 1 1) surface, as shown in Fig. 4(b). They were estimated to be $E_m = 76$ meV and $E_e = 0.96$ eV, respectively. With these two energy barriers and procedures described in Note S1, we evaluated $\nu_s$ and $\nu_e$ as expressed in Eqs. (S1) and (S2), which depend on the area

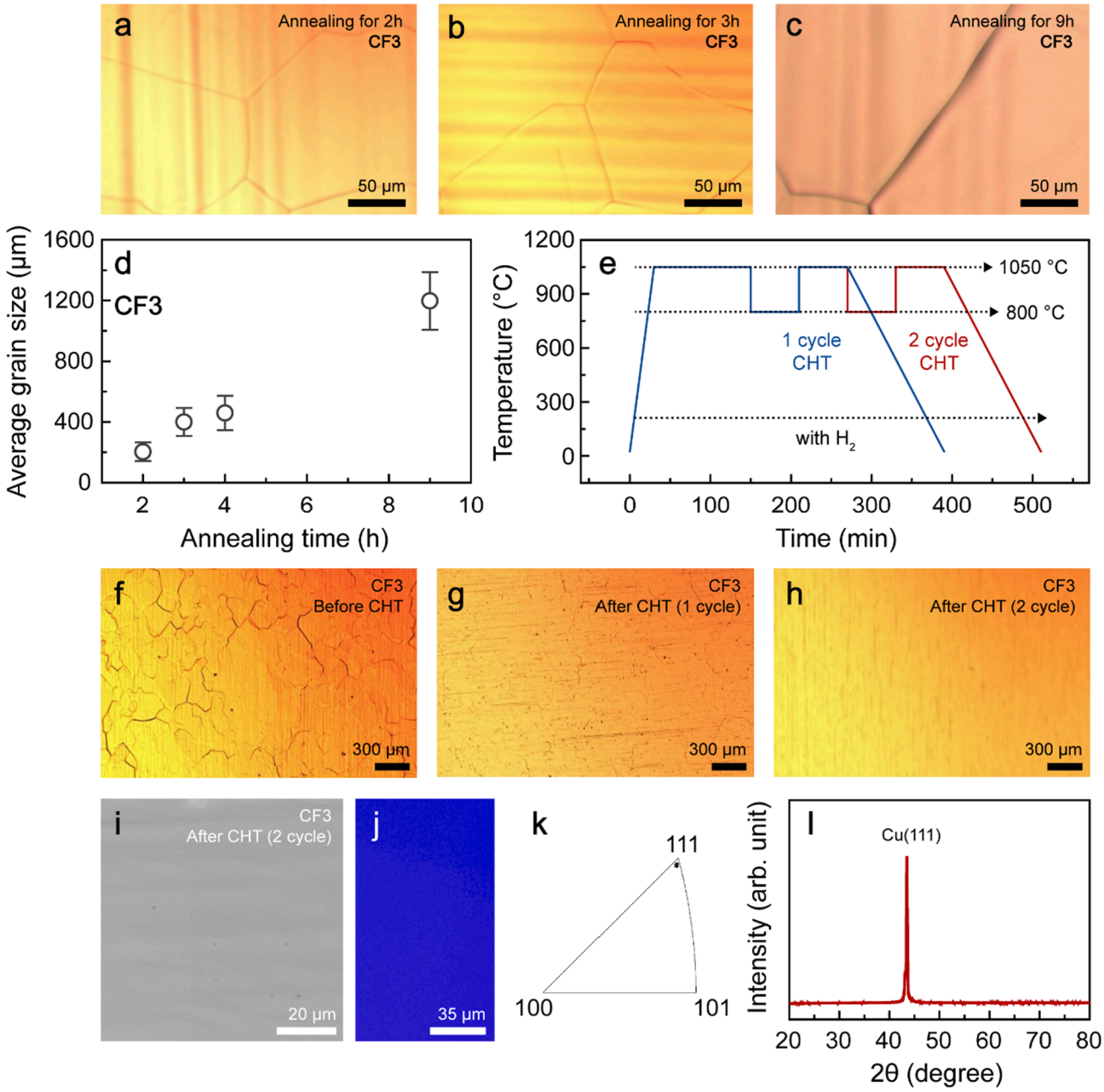


**Fig. 3.** Representative optical microscope images of groove evolution of the oxygen deficient CF3 with prolonged annealing time for (a) 2 h, (b) 3 h, and (c) 9 h. (d) A plot of average grain size of recrystallized CF3 as a function of annealing time. (e) Experimental schedule for the CHT procedure to attain single crystalline CFs. Optical microscope images of CF3 (f) before CHT, (g) after 1 cycle CHT, and (h) 2 cycles CHT. (i) A representative SEM image, (j) ODF and (k) IPF maps acquired from EBSD and (l) a XRD pattern for CF3 with 2 cycles CHTs.

density $\sigma$ of Cu adatoms and the line density $\lambda$ of dangling Cu atoms. Then, we presumed the conditions for CHT as follows. Fig. 4(c) shows dynamic equilibrium conditions of balancing between $\nu_s$ and $\nu_e$ at $T =$ 800 (blue line) and 1050℃ (red line), which are represented by the linear relations of $\sigma$ and $\lambda$. For $\nu_s > \nu_e$ corresponding to the region above each equilibrium line, more Cu adatoms are reaching any groove edges than dangling Cu atoms escaping from groove edges, whereas the other way around for $\nu_s < \nu_e$ corresponding to the region below each line. In other words, grooves will be filled in the conditions corresponding to the region above each equilibrium line, whereas they will be widened in those below it. Thus, the experimental condition of the CHT would fall into the shaded region in-between the two lines. Our simulation results imply that a decrease in the annealing temperature allows relatively boosted diffusion of Cu atoms from surface to groove for filling grooves, regardless of structural features of grain boundaries (Γ). They also provide us with crucial insight into the importance of lower temperature annealing for filling grooves. The low-temperature annealing process (800 °C) for filling grooves caused by the diffusion of Cu atoms was periodically combined with the high-temperature annealing process (1050 °C) for recrystallization of Cu (cyclic heat treatment (CHT)), as demonstrated in Fig. 3(e) [24,25]. It should be highlighted that the deep grooves of CF3 were blurred indisputably with applying 1 cycle of CHT and disappeared completely with 2 cycles of CHT, as presented in Fig. 3 (f–h). In addition, we implemented CHT for CF4, resulting in that the (1 0 0)-oriented surface and the grain size were invariant, as shown in Fig. S3. Fig. 3(i–l) exhibits a representative SEM image, ODF, IPF maps, and an XRD pattern acquired from single-crystalline CF3. Consequently, the large (1 1 1) grains were merged into a single crystal caused by

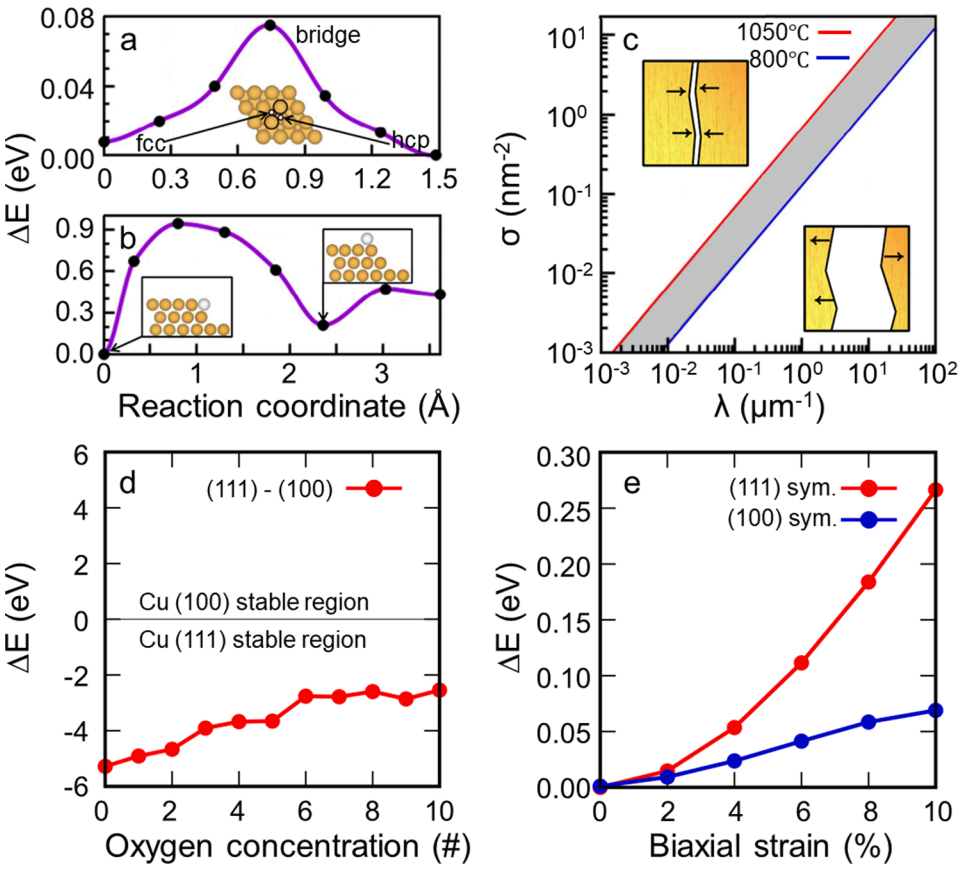


**Fig. 4.** (a) The migration energy barrier of a Cu adatom between nearest neighboring fcc and hcp adsorption sites on a perfect Cu (1 1 1) surface. (Inset) Top view of a (1 1 1) Cu surface indicating neighboring fcc and hcp adsorption sites. (b) The escaping energy barrier of a dangling Cu atom from a groove edge binding site toward nearby adsorption sites on a Cu (1 1 1) surface. (Inset) Side view of a dangling Cu atom (grey sphere) before and after escaping from a groove edge. (c) Result of DFT-based Monte Carlo simulation: the linear relations of the area density $\sigma$ of Cu adatoms on Cu (1 1 1) surface and the line density $\lambda$ of dangling Cu atoms at groove edges at $T = 800$ (blue line) and 1050℃ (red line) representing the dynamic equilibrium conditions of balancing ($\nu_s = \nu_e$) between the reaching rate $\nu_s$ of Cu adatoms to any groove edges and the escaping rate $\nu_e$ of dangling Cu atoms. (Inset) Schematic view diplaying the filling and widening of a groove occuring under any conditions corresponding to above ($\nu_s > \nu_e$) and below ($\nu_s < \nu_e$) each dynamic equilibirum line, respectively. The experimental condition of the CHT would fall into the shaded region in-between the two lines. (d) Total energy difference (ΔE) between O/Cu (1 1 1) and O/Cu(1 0 0) system according to oxygen coverage. (See Fig. S2(a, b) for oxygen adsrobed surface structures.) (e) Relative energies (ΔE) of bulk Cu as a function of biaxial strain applied on the (1 1 1) (red) and (1 0 0) (blue) planes. (For interpretation of the references to colour in this figure legend, the reader is referred to the web version of this article.)

repeated CHT. In addition, transverse (TD) and rolling direction (RD) mapping acquired from EBSD were employed to consolidate the formation of single-crystalline CF3 by CHT, as displayed in Fig. S4.

Several theoretical studies have suggested that thin polycrystalline FCC metals can be recrystallized in a preferential direction by adequate heat treatment [5,6,7,8,13]. However, the experimental results were inconsistent, in which they propose contradictory results depending on their sample preparation processes. In order to unveil a possible mechanism for oxygen-mediated selection of crystallographic orientation, we first calculated the total surface energy variation for oxygen-covered Cu (1 0 0) and Cu(1 1 1) surfaces with various oxygen coverages (0 oxygen atoms (Oxy 0), 6 atoms (Oxy 6), 8 atoms (Oxy 8), and 10 atoms (Oxy 10)), the structures of which are respectively displayed in Fig. S2(a) and (b). Fig. 4(d) shows the energy difference ($\Delta E$) between the O/Cu(1 1 1) and O/Cu(1 0 0) systems as a function of oxygen coverage. For all oxygen concentrations, the surface energy of Cu(1 1 1) is lower than that of Cu (1 0 0), indicating that the Cu(1 1 1) is energetically more favorable than Cu(1 0 0), resulting in the predominant recrystallization of Cu(1 1 1) [8,14,23,26,27], although a gradual decrease in the surface energy difference between O/Cu(1 1 1) and O/Cu(1 0 0) systems is discernible by elevating oxygen coverage, as exhibited in Fig. 4(d). We also investigated the effects of oxygen when oxygen atoms are placed below the surfaces of Cu(1 0 0) and Cu(1 1 1) systems. Let us define $\Delta E_f$ by the formation energy difference between when inserting an oxygen atom into the 1st interlayer and when inserting it into the 2nd interlayers just below the surface in the six-layer slab structure of each system. We calculated $\Delta E_f$ to be 0.44 and –0.18 eV in Cu(1 0 0) and Cu(1 1 1) systems, respectively, implying that oxygen atoms prefer staying inside the Cu(1 0 0) system to escaping out to its surface and the other way around in the Cu(1 1 1) system. We further discovered that oxygen atoms favor forming in dimers rather than isolated individual atoms inside the Cu bulk system and oxygen insertion have the bulk system expand. To compare the stability of the structural symmetries of Cu(1 0 0) and Cu (1 1 1) systems, we explored the strain effect on their total energies while maintaining their structural symmetries representing [1 0 0] and [1 1 1] orientations. As shown in Fig. 4(e), it requires much more energy to preserve the symmetry of the (1 1 1) plane than to preserve that of the (1 0 0) plane as the strain increases. We presume that the oxygen insertion would make a similar effect as the strain. An increase in oxygen concentration leads to the exertion of elastic strain energy, the energy exerted by the presence of lattice mismatch caused by the bonding of alien and host atoms, as well as surface energy in the O/Cu system. Namely, oxygen-induced elastic strain energy enables a decrease in the surface energy difference between O/Cu(1 1 1) and O/Cu(1 0 0) systems, resulting in the recrystallization of Cu(1 0 0). If the oxygen in commercially available CFs was completely eliminated, the surface of CFs can be reconstructed into a (1 1 1) surface, where small grains grew into larger grains *via* abnormal grain growth. Consequently, the (1 1 1) grains merge into a single crystal stimulated by additional CHT involving filling grooves and subsequent recrystallization processes, as illustrated in Fig. S2(c). Conversely, oxygen incorporated CFs preferred to recrystallize the (1 0 0) crystal plane during annealing, in which the residual oxygen seems to affect the grain orientation in the (1 0 0) direction by the exertion of elastic strain energy in the system [10,11]. The size of the (1 0 0) grains was not enlarged additional CHT.

Graphene was synthesized by conventional thermal chemical vapor deposition (TCVD). CF3 and CF4 with 2 cycles of CHT were adopted as catalytic substrates for graphene synthesis to verify a correlation between the Cu domain enlargement and growth aspect of graphene. The graphene coverage on CFs was precisely manipulated by regulating the $CH_4$ flow rate. With graphene grown by adopting 1.5 sccm $CH_4$, the continuous layer was transferred onto a $SiO_2$ (300 nm)/Si(0 0 1) substrate by a poly(methyl methacrylate) (PMMA)-assisted wet transfer technique. Optical microscopy images acquired from graphene grown

on CF3 and CF4 using 0.32 sccm $CH_4$ reveal that the size of the crystalline domains is estimated to be approximately 100 μm, regardless of the sample in Fig. 5(a, b). Unlike the graphene on CF4, it is worth noting that homogeneous orientation of hexagonal graphene domains was distinctly observed for CF3, which hints that the graphene on CF3 is indeed a single crystal. The resonant Raman spectra recorded with an excitation wavelength of 514 nm of graphene on CF3 and CF4 represent the graphene fingerprints involving the G- and 2D-bands are discernible in Fig. 5(c, d). The G-band is associated with normal first-order Raman scattering, involving an electron and the doubly degenerated phonons (iTO and iLO) at the Brillouin zone center. The 2D-band originates from an intervalley double resonance Raman process, involving an electron and two iTO phonons at the *K* point [28]. The absence of the defect-induced D-band for graphene on CF3 reflects defect-less and single-

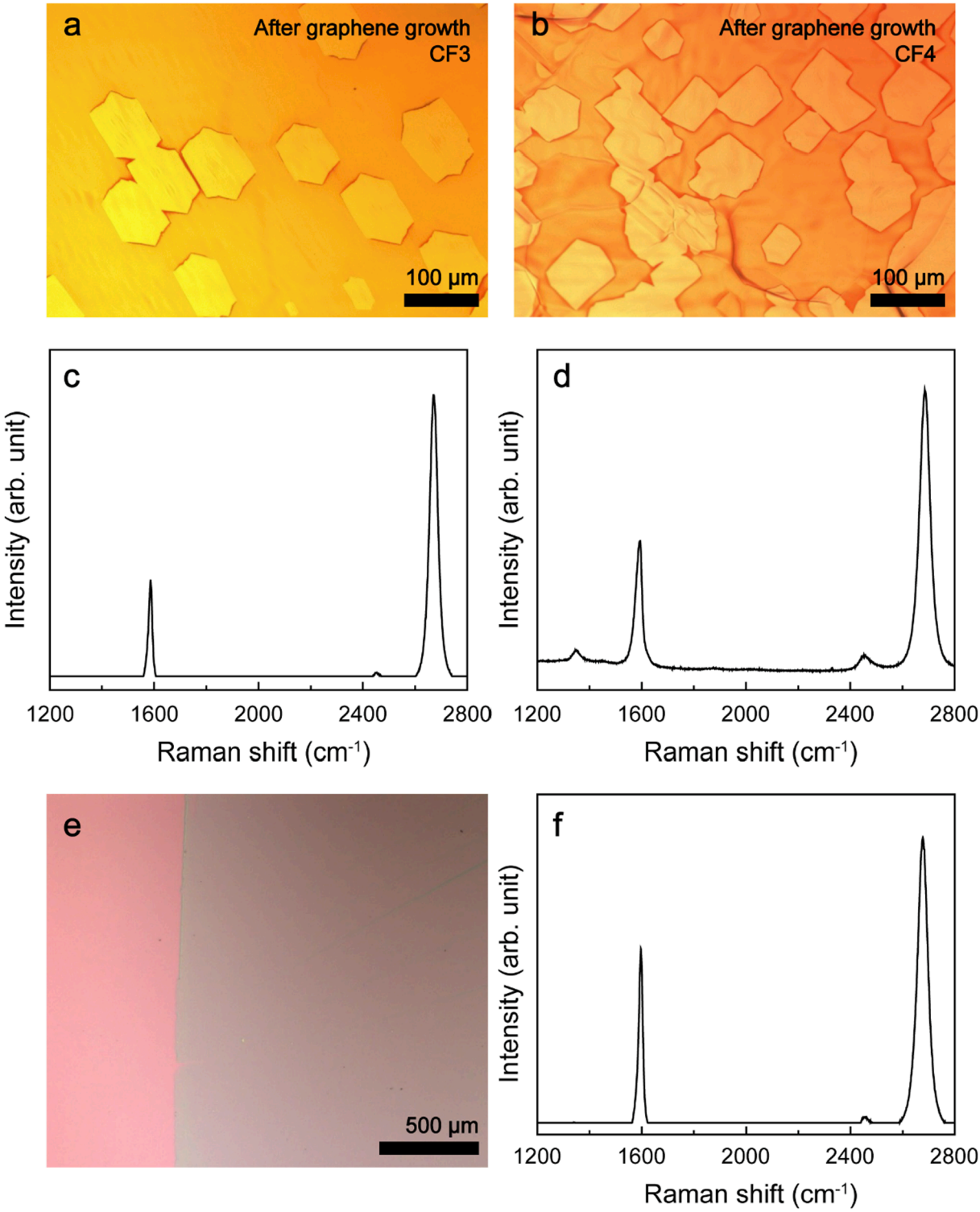


**Fig. 5.** (a,b) Representative optical microscope images of graphene synthesized on CF3 and CF4 using 0.32 sccm $CH_4$ and (c,d) resonant Raman spectra recorded with an excitation wavelength of 514 nm for graphene synthesized on CF3 and CF4. (e) An optical microscope image and (f) Raman spectrum for graphene, synthesized by adopting 1.5 sccm $CH_4$, transferred onto $SiO_2$ (300 nm)/Si(001) using a PMMA-assisted wet transfer technique.

crystalline graphene. The large-area and continuous monolayer graphene was successfully synthesized using 1.5 sccm $CH_4$ injections. After transfer onto a $SiO_2$/Si substrate using a PMMA-assisted wet transfer technique, optical microscopy combined with Raman spectroscopy demonstrated that the structural features of continuous graphene grown on CF3 were well-preserved as shown in Fig. 5(e, f). To verify the large-scale uniformity of single-crystalline graphene synthesized on recrystallized CF3 using 1.5 sccm $CH_4$ injection, spatially resolved Raman mapping (area: 100 × 100 $\mu m^2$) of the intensity of the D- and G-bands Raman active phonon modes was carried out, as displayed in Fig. S5. The nearly negligible intensity of the D-band and virtually no spatial variation in the intensity of the G-band for graphene were distinctly observed, clearly reflecting the excellent structural homogeneity of the sample.

## 4. Conclusion

In summary, we unprecedentedly explored the recrystallization phenomena for Cu grains in a specific direction that can be mainly mediated by the presence of oxygen in the grains. Based on these results, we attained structural transition from polycrystalline CF to single-crystalline CF by eliminating oxygen into the grain by the CHT procedure under a hydrogen atmosphere. We envisage that single-crystalline CFs will be valuably adoptable for the synthesis of large-area single-crystalline graphene and also in many other fields.

### *CRediT authorship contribution statement*

**Hyeong-ku Jo:** Data curation, Writing – original draft. **Hanjin Park:** Data curation, Methodology. **Hyung-June Lee:** Data curation, Methodology. **Garam Bae:** Data curation, Writing – review & editing. **Da Som Song:** Data curation, Methodology. **Ki Kang Kim:** Formal analysis, Writing – review & editing. **Wooseok Song:** Formal analysis, Writing – review & editing, Supervision. **Cheolho Jeon:** Data curation, Writing – review & editing. **Ki-Seok An:** Writing – review & editing. **Young-Kyun Kwon:** Conceptualization, Writing – review & editing, Supervision. **Chong-Yun Park:** Conceptualization, Writing – review & editing, Supervision.

## Declaration of Competing Interest

The authors declare that they have no known competing financial interests or personal relationships that could have appeared to influence the work reported in this paper.

## Acknowledgements

This research was supported by Basic Science Research Program through the National Research Foundation of Korea (NRF) funded by the MOE and MSIT (2017R1D1A1B0334168, 2019R1A2C1005417, and 2020R1A5A6017701) and Multi-Ministry Collaborative R&D Program through the National Research Foundation of Korea (NRF) funded by KNPA, MOTIE, ME, NFA (NRF-2017M3D9A1073858). A portion of our computational work was done using the resources of the KISTI Supercomputing Center (KSC-2020-CRE-0260).

## Appendix A. Supplementary material

Supplementary data to this article can be found online at https://doi.org/10.1016/j.apsusc.2022.152585.

## References

[1] B. Hu, H. Ago, C.M. Orofeo, Y. Ogawa, M. Tsuji, On the nucleation of graphene by chemical vapor deposition, New J. Chem. 36 (1) (2012) 73–77.
[2] X.i. Mi, V. Meunier, N. Koratkar, Y. Shi, Facet-insensitive graphene growth on copper, Phys. Rev. B 85 (15) (2012), https://doi.org/10.1103/PhysRevB.85.155436.
[3] C.-M. Seah, S.-P. Chai, A.R. Mohamed, Mechanisms of graphene growth by chemical vapour deposition on transition metals, Carbon 70 (2014) 1–21.
[4] X. Xu, Z. Zhang, J. Dong, D. Yi, J. Niu, M. Wu, L.i. Lin, R. Yin, M. Li, J. Zhou, S. Wang, J. Sun, X. Duan, P. Gao, Y. Jiang, X. Wu, H. Peng, R.S. Ruoff, Z. Liu, D. Yu, E. Wang, F. Ding, K. Liu, Ultrafast epitaxial growth of metre-sized single-crystal graphene on industrial Cu foil, Sci. Bull. 62 (15) (2017) 1074–1080.
[5] S. Jin, M. Huang, Y. Kwon, L. Zhang, B.-W. Li, S. Oh, J. Dong, D.a. Luo, M. Biswal, B.V. Cunning, P.V. Bakharev, I. Moon, W.J. Yoo, D.C. Camacho-Mojica, Y.-J. Kim, S.H. Lee, B. Wang, W.K. Seong, M. Saxena, F. Ding, H.-J. Shin, R.S. Ruoff, Colossal grain growth yields single-crystal metal foils by contact-free annealing, Science 362 (6418) (2018) 1021–1025.
[6] J. Hu, J. Xu, Y. Zhao, L. Shi, Q. Li, F. Liu, Z. Ullah, W. Li, Y. Guo, L. Liu, Roles of Oxygen and Hydrogen in Crystal Orientation Transition of Copper Foils for High-Quality Graphene Growth, Sci. Rep. 7 (2017) 45358.
[7] V.L. Nguyen, B.G. Shin, D.L. Duong, S.T. Kim, D. Perello, Y.J. Lim, Q.H. Yuan, F. Ding, H.Y. Jeong, H.S. Shin, S.M. Lee, S.H. Chae, Q.A. Vu, S.H. Lee, Y.H. Lee, Seamless Stitching of Graphene Domains on Polished Copper (111) Foil, Adv. Mater. 27 (8) (2015) 1376–1382.
[8] L. Brown, E.B. Lochocki, J. Avila, C.-J. Kim, Y. Ogawa, R.W. Havener, D.-K. Kim, E. J. Monkman, D.E. Shai, H.I. Wei, M.P. Levendorf, M. Asensio, K.M. Shen, J. Park, Polycrystalline Graphene with Single Crystalline Electronic Structure, Nano Lett. 14 (10) (2014) 5706–5711.
[9] Y.-N. Wen, J.-M. Zhang, Surface energy calculation of the fcc metals by using the MAEAM, Solid State Commun. 144 (3-4) (2007) 163–167.
[10] X. Duan, O. Warschkow, A. Soon, B. Delley, C. Stampfl, Density functional study of oxygen on Cu(100) and Cu(110) surfaces, Phy. Rev. B 81 (7) (2010), https://doi.org/10.1103/PhysRevB.81.075430.
[11] M.M. Ferrer, G.S.L. Fabris, B.V. de Faria, J.B.L. Martins, M.L. Moreira, J. R. Sambrano, Quantitative evaluation of the surface stability and morphological changes of $Cu_2O$ particles, Heliyon 5 (10) (2019) e02500, https://doi.org/10.1016/j.heliyon.2019.e02500.
[12] N. Reckinger, X. Tang, F. Joucken, L. Lajaunie, R. Arenal, E. Dubois, B. Hackens, L. Henrard, J.-F. Colomer, Oxidation-assisted graphene heteroepitaxy on copper foil, Nanoscale 8 (44) (2016) 18751–18759.
[13] Y.-P. Hsieh, D.-R. Chen, W.-Y. Chiang, K.-J. Chen, M. Hofmann, Recrystallization of copper at a solid interface for improved CVD graphene growth, RSC Adv. 7 (7) (2017) 3736–3740.
[14] Z.R. Robinson, P. Tyagi, T.M. Murray, C.A. Ventrice, S. Chen, A. Munson, C. W. Magnuson, R.S. Ruoff, Substrate grain size and orientation of Cu and Cu–Ni foils used for the growth of graphene films, J. Vac. Sci. Technol. A 30 (1) (2012) 011401, https://doi.org/10.1116/1.3663877.
[15] W. Kohn, L.J. Sham, Self-Consistent Equations Including Exchange and Correlation Effects, Phys. Rev. 140 (4A) (1965) A1133–A1138.
[16] G. Kresse, J. Hafner, Ab initio molecular dynamics for open-shell transition metals, Phys. Rev. B 48 (17) (1993) 13115–13118.
[17] G. Kresse, J. Furthmüller, Self-interaction correction to density functional approximation for many electron systems, Phys. Rev. B 54 (1996) 11169–11186.
[18] P.E. Blöchl, Projector augmented-wave method, Phys. Rev. B 50 (24) (1994) 17953–17979.
[19] G. Kresse, D. Joubert, From ultrasoft pseudopotentials to the projector augmented-wave method, Phys. Rev. B 59 (3) (1999) 1758–1775.
[20] J.P. Perdew, K. Burke, M. Ernzerhof, Generalized gradient approximation made simple, Phys. Rev. Lett. 77 (18) (1996) 3865–3868.
[21] H.J. Monkhorst, J.D. Pack, Special points for Brillouin-zone integrations, Phys. Rev. B 13 (12) (1976) 5188–5192.
[22] J. Liu, Q. Liu, J. Baca, G. Xu, C. Rochford, R. Lu, C.M. Edwards, C.L. Berrie, V. A. Maroni, J. Wu, Direct graphene growth on (111) $Cu_2O$ templates with atomic Cu surface layer, Carbon 95 (2015) 608–615.
[23] C.E. Murray, R. Rosenberg, C. Witt, M. Treger, I.C. Noyan, Evolution of strain energy during recrystallization of plated Cu films, J. Appl. Phys. 113 (20) (2013) 203515, https://doi.org/10.1063/1.4807409.
[24] T. Omori, T. Kusama, S. Kawata, I. Ohnuma, Y. Sutou, Y. Araki, K. Ishida, R. Kainuma, Abnormal Grain Growth Induced by Cyclic Heat Treatment, Science 341 (6153) (2013) 1500–1502.
[25] T. Kusama, T. Omori, T. Saito, S. Kise, T. Tanaka, Y. Araki, R. Kainuma, Ultra-large single crystals by abnormal grain growth, Nat. Comm. 8 (2017) 354.
[26] C.C. Wong, H.I. Smith, C.V. Thompson, Surface-energy-driven secondary grain growth in thin Au films, Appl. Phys. Lett. 48 (5) (1986) 335–337.
[27] C.V. Thompson, R. Carel, Stress and grain growth in thin films, J. Mech. Phys. Solids 44 (5) (1996) 657–673.
[28] L.M. Malard, M.A. Pimenta, G. Dresselhaus, M.S. Dresselhaus, Raman spectroscopy in graphene, Phys. Rep. 473 (5-6) (2009) 51–87.